Article

Prediction of Self-Sustained Oscillations of an Isothermal Impinging Slot Jet

Bruno A. C. Barata *, Jorge E. P. Navalho and José C. F. Pereira

IDMEC, Instituto Superior Técnico, Universidade de Lisboa, 1649-004 Lisboa, Portugal
* Correspondence: bruno.a.c.barata@tecnico.ulisboa.pt

Abstract: The present results are focused on the self-sustained oscillations of a confined impinging slot jet and their role in the flow structure and modeling requirements. Unsteady laminar, large-eddy simulation (LES), and Reynolds-averaged Navier–Stokes (RANS) predictions of an isothermal confined impinging jet were validated for several nozzle-to-plate ratios ($H/B = 4$–15) and for laminar ($Re = 340$ and 480) and turbulent ($Re = 10^4$–2.7×10^4) conditions. The impinging flow structure was found to be highly influenced by the H/B ratio. For high ratios ($H/B > 5$), the studied steady RANS turbulence models could not satisfactorily predict the high diffusion reported experimentally in the jet-impinging influence zone. The failure of these models has been attributed to the modeling issues of turbulence closures. However, for $H/B = 8$, unsteady laminar 3D and LES calculations were verified, and a sinuous oscillation mode was developed, revealing self-sustained oscillations and the display of periodic flapping of the impinging jet in good agreement with the experiments. The predicted flapping oscillation is one of the reasons for the higher diffusion near the impingement wall, which was verified in several time-averaged experimental studies. The presence of jet flapping matters for clarifying the already long discussion on the RANS model's validation in predicting impinging jets with high H/B ratios, adding justification to the failure of these turbulence models. This unsteady behavior is correctly computed through LES.

Keywords: impinging slot jet; flapping jet; global oscillations; laminar; RANS; LES

1. Introduction

Impinging jets are used in many engineering applications such as electronic equipment, drying of continuous sheets of materials, controlling the thickness in thin film coating, cooling turbine blades, or combustion chambers for aeronautics (see, e.g., [1–3]). The heat transfer enhancement due to impinging jets has been reviewed in detail in the literature (see, e.g., [4–7]). Moreover, impinging jets may act as air curtains, limiting the heat and mass transfer between two different zones. Applications of these sealing curtains can be found in food industries, containment of polluted zones, building energy-saving, and fire protection, among other applications (see, e.g., [8–12]).

Impinging jets can be classified into open or confined jets. The first is released into an open space and the second into a confined space, such as a plane channel or a cylinder in which the pressure field is constrained by the wall confinement. Several impinging jet configurations have been investigated, including jets released from round or slot nozzles, different types of jet arrays, impinging on flat and curved surfaces, and normal and inclined impingement. This work focuses on the geometry of a confined single jet from a slot nozzle of a width B impinging on the flat surface of an open-ended channel of a height H.

Moreover, the flow field created by the jet impingement can be divided into various zones (depending on the nozzle-to-plate ratio H/B), each with its own flow features. Figure 1 depicts the jet's normal fluid-dynamic characteristics, mainly revealing four distinct regions.
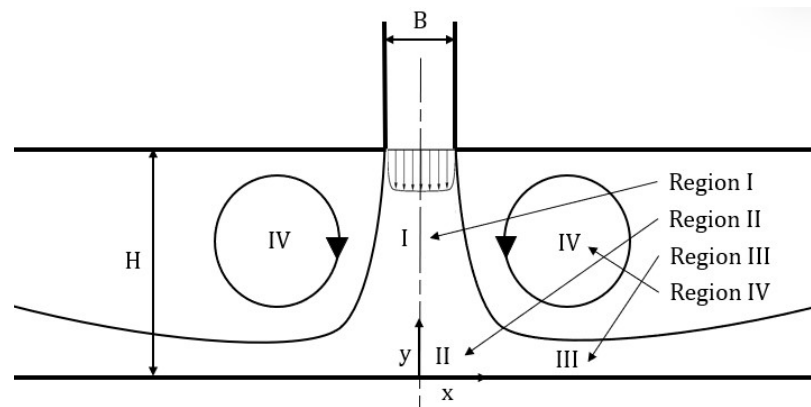
Figure 1. Geometry of a 2D confined slot impinging jet.

The free jet (Region I) is the region of the flow where the impingement surface has no impact on the flow structure, presenting the typical behavior of a free jet. This region can be divided into a potential core (within which the uniform exit velocity is maintained) and a transition or developed zone. The potential core is the zone of flow establishment, where it is surrounded by a free shear layer in which the jet entrains the ambient fluid and slowly expands.

Near the plate, the vertical velocity of the flow decays quickly, and the jet is deflected from its normal direction in a region called the stagnation region (Region II). Therefore, contrary to a free jet, the flow is influenced by the impingement surface and is decelerated in the normal (y) direction and accelerated in the transverse (x) direction due to a streamwise stabilizing pressure gradient near the stagnation point. This acceleration in the transverse direction creates a wall jet along the bottom wall. In the wall jet region (Region III), the pressure gradient effect no longer holds, and turbulence can increase significantly. Thus, accelerating flow in the stagnation zone converts into a decelerating wall jet. Furthermore, in the case of a confined impinging jet, a recirculation region (Region IV) arises, owing to both the impinging jet and the wall jet, as seen in Figure 1.

Some of the above-mentioned zones may no longer be present when the plate is near the nozzle exit, (i.e., for small H/B ratios). If the plate is placed at very short distances from the nozzle, the high static pressure in the stagnation area strongly affects the flow development up to the nozzle exit.

Experimental investigation of round- and slot-nozzle impinging jets has been carried out to study the effect of the enhancement of convective transport phenomena. Tu and Wood [13] as well as Zhe and Modi [14] reported on the role of the H/B and Reynolds number for an impingement wall's distances from $H/B = 2$ to 9.2 and jet Reynolds numbers from 10^4 to 3×10^4. In addition, for a Reynolds number of 2×10^4 and H/B ratios of 4 and 9.2, Ashforth-Frost et al. [15] showed that when the impingement plate was located within the potential core of the jet, the turbulence levels increased in the stagnation area and in the wall jet, demonstrating that the transition to a turbulent wall jet occurred. However, when the impingement plate was placed in the developing jet, the measurements revealed that the jet was effectively turbulent at the stagnation point. Consequently, the influence of the H/B on the flow structure of a laminar, transitional, or turbulent impinging jet is still an open subject of research for finding the modeling requirements to reproduce the same order of accuracy under a change in the H/B parameter.

The relevance of impinging jets on heat transfer applications has also given rise to numerous numerical Reynolds-averaged Navier–Stokes (RANS) studies over the last few decades, and it is still a topic of interest nowadays [16,17]. Dutta and Dewan [18] studied the turbulent impinging jet flow at a Reynolds number of 2×10^4, applying several RANS turbulence models. Only for $H/B = 4$ did the standard and shear stress transport (SST) k-ω models exhibit good agreement with the experimental data in terms of fluid flow and heat transfer predictions. For $H/B = 9.2$, the models forecasted an inaccurate trend in the

surface Nusselt number distributions. Achari and Das [19] also compared several RANS-based turbulence models: the standard k-ε model, the low Reynolds number k-ε models suggested by Launder and Sharma as well as Yang and Shih, and the standard k-ω models. For $H/B = 4$, the predictions followed the distribution of pressure on the impingement and the overall velocity field closely. However, for $H/B = 9$, the computational results overpredicted the streamwise velocity up to $y/B = 0.4$, after which they underpredicted when compared with the experimental results. Many other works also noticed the poor performance of RANS models for impinging jet simulations at large H/B distances, in contrast with their good performance for small H/B distances (see, e.g., [20–26]). The highlighted justification was the strong underestimation by RANS of the turbulent mixing in the shear layer of the jet, which is characteristic of impinging jet simulations at large H/B distances, in contrast with their good prediction for small H/B distances, for which the error in the turbulent mixing by RANS models was found to be minor. Dewan and Dutta [27] also pointed out the influence of the flow complexity in the stagnation region, the many arbitrary coefficients inherent in models, the poor performance of the wall and damping functions, and the quasi-periodic impingement of large-scale coherent structures in the impingement wall. Consequently, erroneous predictions of the stagnation zone flow and overprediction of the stagnation point heat transfer are obtained for high H/B values.

Flow visualization studies for round impinging jets demonstrated that the flow is not statistically stationary (see, e.g., [28–31]). Khayrullina et al. [11] investigated experimentally an isothermal plane-turbulent impinging jet on a horizontal plane for an H/B equal to 22.5 and 45 at moderate Reynolds numbers (from 7.2×10^3 to 1.35×10^4). Snapshots of the dye-visualized jet indicated the development of the jet's flapping as the jet was moving from side to side in the region close to the impingement plate. The jet's flapping was also reported in earlier studies, where the instantaneous velocity fluctuations on opposite sides of a subsonic plane jet were measured [32]. The results indicated that there was flapping of the jet with a Strouhal number of 5.5×10^{-3} based on B.

The unsteadiness of impinging plane jets originates from the primary vortices caused by shear layer instability of the Kelvin–Helmholtz type. The unsteady flow is dominated by these primary vortices, which increase the complexity of the impinging jet flow as they approach the wall. The transition process of jets is dominated by two different characteristics of instability modes that have different length scales and actuate into two different flow regions. In the plane jet, Kelvin–Helmholtz vortices are generated by the jet shear layer instability mode from the initial shear layer to the end of the potential core. These structures are then convected downstream toward the impinging wall. At the end of the potential core, the main instability mode is the preferred mode (see, e.g., [33,34]).

The dynamics of a confined laminar plane jet impinging on a flat plate in a channel was studied by Varieras et al. [35]. The experimental study was carried out for jet Reynolds numbers from 10^2 to 10^3 and H/B values from 4 to 9. It was found that the flow was steady for very confined jets regardless of the Reynolds number. For these cases, the flow presented a symmetrical shape in terms of the jet axis and was characterized by the existence of recirculation zones along the channel walls. However, the dynamics was reported to be drastically different for less-constrained jets. In particular, above a certain Reynolds number, the flow was found to bifurcate in the form of an oscillating flapping mode of the impinging jet. It was acknowledged that the frequency of global oscillations scales with H/V_j and that H is the crucial length scale for the study of self-sustained global oscillations. Regardless of the aspect ratio and Reynolds number, the Strouhal number, based on H, was verified to be approximately 0.45.

For turbulent impinging jets, the flow complexity increases due to the interactions of the vorticity and turbulence dynamics [36–39]. For small H/B distances, a secondary maximum in the instantaneous Nusselt number is observed in the separation region. The secondary maximum is attributed by direct numerical simulation (DNS) predictions to the engulfing motion around the secondary vortex, which reduces the thickness of the thermal boundary layer [40–45]. In addition, the large-eddy simulation (LES) instantaneous

data of impinging jets illustrates a number of significant dynamical flow structures, such as Kelvin–Helmholtz instability in the shear layer and the occurrence of counter-rotating vortices in the impingement region (see, e.g., [46]). Bisoi et al. [47] predicted the coherent structures' evolution and final disintegration to smaller vortices for a transitional slot jet at a Reynolds number of 4×10^3. Shukla and Dewan [48] verified LES predictions for turbulent slot jet impingement heat transfer with a small nozzle-to-plate distance ($H/B = 4$). Four sub-grid stress (SGS) models were considered for a Reynolds number of 2×10^4: Smagorinsky, WALE, k-equation, and dynamic k-equation. The results using the four SGS models mirrored the trends of the experimental data, particularly the velocity and turbulence profiles. Using the four SGS models, a secondary peak in the Nusselt number was observed. In this way, it has been demonstrated that the LES is capable of capturing small-scale dynamics in complicated flow zones.

Hybrid RANS/LES models have also been considered to overcome the poor performance of RANS models for impinging jet simulations at large H/B distances. Kubacki and Dick [49] simulated plane-impinging jets with $H/B = 10, 9.2$, and 4 at $Re = 1.35 \times 10^4$ and 2×10^4 using the k–ω-based hybrid RANS/LES models and RANS k–ω model. The hybrid RANS/LES models were found to be better for the simulation of plane-impinging jets at high H/B distances since, in contrast to RANS, the hybrid approaches were able to simulate the turbulent flow dynamics in the impacting jet's shear layers. Detached eddy simulation (DES) and a partially averaged Navier–Stokes (PANS) hybrid RANS/LES model, both based on the k–ω RANS turbulence model, were analyzed by Kubacki et al. [50] for the simulation of plane-impinging jets at a high H/B distance ($H/B = 10$, $Re = 1.35 \times 10^4$) and a low H/B distance ($H/B = 4$, $Re = 2 \times 10^4$), and a similar conclusion was achieved. Wu and Piomelli [51] found that unsteady RANS (URANS) solutions do not yield a reliable prediction of the development of the azimuthal vortices, a well-known shortcoming of most eddy viscosity turbulence models in this type of configuration, while variational multi-scale large-eddy simulation (VMLES) and DES predict vortex decay.

Although it is widely documented in the literature, high Reynolds number impinging jet flows (with industrial representativeness) are not sufficiently well-known, particularly for the influence of various parameters such as the impingement distance, confinement, and Reynolds number. In fact, the plane-impinging jet features different flow patterns with the H/B ratio. Consequently, three plane-impinging jet classes were defined by So et al. [52] according to the actual H/B ratio: a stable impinging jet for $H/B \leq 4$, periodically stable impinging jet for $4 < H/B < 11$, and unstable impinging jet for $H/B \geq 11$. In addition, the confined impinging jet forms a plane channel between the parallel confining top plate and the target plate, subject to open boundary end extremities, and results in a more complicated flow structure. The numerical modeling of the impinging jet becomes a challenging task due to these factors. As pointed out by Thysen et al. [12], the impinging jets are still not fully understood due to their highly unsteady nature.

For the turbulent impinging jet, RANS-based turbulence models lack generality in predicting impinging flows, and URANS is unable to predict the generation and evolution of coherent structures in the mixing layer and their effect on the structure of the impinging jet and level of heat transfer in the stagnation region. DNS at moderate Reynolds numbers is used for validation of LES capability to capture the small-scale dynamics often associated with the discussion of the second peak in impinging heat transfer [43,53]. However, LES requires a grid to be fine enough in the shear layer of the jet and for the formation of the secondary vortices in the near-wall region. The inlet jet boundary conditions may also modify the impinging jet development. Usually, a natural inflow condition is used, characterized by an imposed flat-top profile and random noise. However, if a forced inflow condition (with a streamwise time-dependent sinusoidal disturbance and a spatial periodic disturbance) is imposed on a steady profile, it promotes a pulsation frequency with significant effects on the formation and size of structures and, consequently, on their dynamics [54–56]. Other practices, such as adding coaxial flow or using a top transpired plate to replace the jet entrainment flow, allow the shortening of the size of the com-

putational domain but prevent the direct comparison of different LES simulations and require the analysis of the forced mechanism used. Similarly, the DNS study performed by Jaramillo et al. [57] for a confined impinging jet revealed that the main recirculating flow cannot be captured well unless the outflow is placed at least at approximately 40 nozzle widths from the jet's centerline, suggesting that previous experimental data may not be adequate to study the flow configuration far from the jet.

For the laminar impinging jet, fewer investigations have been conducted. Using the time-resolved particle image velocimetry (PIV) technique, Kim et al. [58] found that the jet remains steady up to a Reynolds number of 404, and with the increase in the Reynolds number, vortical structures start to develop in the shear layer. Chatterjee and Tarbell [59] showed that flow unsteadiness appearing for $Re > 130$ is a consequence of the bifurcation of the steady flow to an unstable branch of steady solutions, while Chiriac and Ortega [60] predicted that the critical Reynolds number was located between 585 and 610. The critical Reynolds number for the onset of unsteady flow is dependent on several factors which are not well known, apart from the confined impinging jet. The asymmetry in the formation of the vortex sheets promotes jet deformation and induces a low-frequency lateral jet "flapping" instability. Consequently, the lack of detailed knowledge about the birth of the oscillations that trigger the lateral flapping of the jet is also an identified problem. DNSs of the laminar impinging jet flow field are relatively few and are required to show the time-dependent behavior for certain aspect ratios and Reynolds number combinations.

The objective of this work is to study a confined slot turbulent jet impinging normally into a flat surface by investigating the effect of the H/B ratio on the flow structure. The performance of several RANS turbulence models is evaluated for various H/B ratios and compared with available experimental data. Subsequently, through LES, the dynamics of the jet is analyzed, paying particular attention to some non-stationarity of the flow that can jeopardize the performance of some widely applied RANS turbulence models. More concretely, the self-sustained oscillations reported experimentally for a laminar impinging jet are predicted and validated by means of DNS. Subsequently, this unsteady phenomenon is also predicted by LES for a turbulent jet, showing that the presence of this type of oscillation matters for clarifying the already long discussion on the RANS model's accuracy to predict impinging jets with high H/B ratios.

Thus, this work has three purposes:

(1) Studying a plane-impinging jet laminar fluid flow in detail by means of DNS and the turbulent flow with LES;
(2) Assessing the ability in terms of accuracy of different RANS models in the description of plane-impinging jets and presenting a detailed evaluation of them according to their capability to predict impinging jet flows;
(3) Analyzing the self-sustained oscillations in laminar and turbulent isothermal impinging slot jets, relating their role in the complex flow characteristics mentioned above.

This paper is organized as follows. Section 2 presents the governing equations and the turbulence models. Then, Section 3 gives details about the flow configuration and the numerical methods, including the boundary conditions. After a brief presentation of the laminar simulations in Section 4, a set of results is presented for the RANS and LES comparison to investigate the ability of RANS to reproduce both low- and high-H/B impinging jet confinement in comparison to the experimental results. Instantaneous flow visualizations are also used to highlight the crucial role of the flapping jet in the impinging region. The main conclusions of this study are provided in Section 5.

2. Mathematical Modeling

2.1. Direct Numerical Simulation

For the direct numerical simulation of laminar impinging jet incompressible fluid flow, the unsteady 3D Navier–Stokes equations are used together with the continuity equation

(see Equations (1) and (2)). In these equations, the index $i = 1, 2, 3$ refers to the x, y, and z directions, respectively:

$$\rho \frac{\partial}{\partial x_i}(u_i) = 0 \tag{1}$$

$$\rho \frac{\partial}{\partial t}(u_i) + \rho \frac{\partial}{\partial x_j}(u_i u_j) = -\frac{\partial p}{\partial x_i} + \mu \frac{\partial}{\partial x_j}\left[\left(\frac{\partial u_i}{\partial x_j} + \frac{\partial u_j}{\partial x_i}\right)\right] \tag{2}$$

2.2. Large-Eddy Simulation

For the LES of turbulent impinging jet flow, the Navier–Stokes equations are filtered with a top hat filter from the finite volume method used. The sub-grid scales are filtered with scales less than the filter size Δ. The filtered continuity and Navier–Stokes equations are shown in Equations (3) and (4), respectively:

$$\frac{\partial \bar{u}_i}{\partial x_i} = 0 \tag{3}$$

$$\frac{\partial}{\partial t}(\bar{u}_i) + \frac{\partial}{\partial x_j}(\bar{u}_i \bar{u}_j) = -\frac{\partial \bar{p}}{\partial x_i} + \frac{1}{Re_B}\frac{\partial^2 \bar{u}_i}{\partial x_j^2} - \frac{\partial \tau_{ij}}{\partial x_j} \tag{4}$$

In LES, the sub-grid scale (SGS) stresses resulting from the filtering procedure are unknown, and modeling is required. The Boussinesq hypothesis is used in the sub-grid scale turbulence models, which compute the sub-grid-scale turbulent stresses from Equation (5), where μ_t is the turbulent viscosity at the sub-grid scale:

$$\tau_{ij} - \frac{1}{3}\tau_{kk}\delta_{ij} = -2\mu_t \bar{S}_{ij} \tag{5}$$

The isotropic component of the sub-grid-scale stresses (τ_{kk}) is added to the filtered static pressure term rather than being modeled. For the resolved scale, $\bar{S}_{ij}$ is the rate-of-strain tensor defined by Equation (6):

$$\bar{S}_{ij} \equiv \frac{1}{2}\left(\frac{\partial \bar{u}_i}{\partial x_j} + \frac{\partial \bar{u}_j}{\partial x_i}\right) \tag{6}$$

2.2.1. Smagorinsky–Lilly Model

In the Smagorinsky–Lilly model [61], the eddy viscosity is modeled by Equation (7), where L_S is the mixing length for the sub-grid scale (computed by Equation (8)) and $|\bar{S}| \equiv \sqrt{2\bar{S}_{ij}\bar{S}_{ij}}$:

$$\mu_t = \rho L_S^2 |\bar{S}| \tag{7}$$

$$L_s = \min(\kappa d, C_s \Delta) \tag{8}$$

In Equation (8), $\kappa = 0.41$ is the von Kármán constant, d is the distance to the closest wall, C_s is the Smagorinsky constant, and Δ is the local grid scale.

In the inertial subrange, Lilly [62] estimated a value of 0.23 for homogeneous isotropic turbulence. However, in the presence of the mean shear and transitional flows near the solid boundary, this value was found to induce excessive damping of large-scale fluctuations. In other words, it is not a universal constant, which is the model's most fundamental flaw.

2.2.2. Dynamic Smagorinsky–Lilly Model

Germano et al. [63], and later Lilly [62], devised a method for dynamically computing the Smagorinsky constant (C_s) based on the information supplied by the resolved scales of motion. As a result, the dynamic approach eliminates the requirement for the definition model constant in advance.

In short, the dynamic process consists of applying a second filter to the equations of motion (called the test filter). The new filter width is twice that of the grid filter. Both filters generate a resolved flow field, and the difference between them is the contribution of small scales, whose size is in between the two filters [64]. The model constant is then calculated using the information relevant to these scales.

At the test filtered field level, the SGS stress tensor is expressed by Equation (9):

$$T_{ij} = \overline{\rho u_i u_j} - \left(\widehat{\rho} \widehat{u_i} \widehat{\rho} \widehat{u_j} / \widehat{\rho} \right) \tag{9}$$

Through the assumption of scale similarity, both τ_{ij} and T_{ij} are modeled similarly using the Smagorinsky–Lilly model. Their modeling is expressed in Equations (10) and (11), respectively, where the coefficient C ($C = C_s^2$) is assumed to be the same and independent of the filtering process:

$$\tau_{ij} = -2C\bar{\rho}\Delta^2 \widetilde{S} \mid \left(\widetilde{S}_{ij} - \frac{1}{3} \widetilde{S}_{kk} \delta_{ij} \right) \tag{10}$$

$$T_{ij} = -2C\hat{\bar{\rho}}\hat{\Delta}^2 |\hat{\widetilde{S}}| \left(\hat{\widetilde{S}}_{ij} - \frac{1}{3} \hat{\widetilde{S}}_{kk} \delta_{ij} \right) \tag{11}$$

The relation between the grid-filtered SGS and the test-filtered SGS is expressed by the Germano identity (see Equation (12)):

$$L_{ij} = T_{ij} - \hat{\tau}_{ij} = \overline{\rho \widetilde{u_i} \widehat{\widetilde{u_j}}} - \frac{1}{\hat{\bar{\rho}}} \left(\overline{\rho} \hat{\widetilde{u_i}} \overline{\rho} \hat{\widetilde{u_j}} \right) \tag{12}$$

By substituting the grid filter Smagorinsky–Lilly model and Equation (11) into Equation (12), Equation (13) is derived to solve for C, in which M_{ij} is expressed in Equation (14):

$$C = \frac{\left(L_{ij} - L_{kk}\delta_{ij}/3 \right) M_{ij}}{M_{ij} M_{ij}} \tag{13}$$

$$M_{ij} = -2 \left(\hat{\Delta}^2 \hat{\bar{\rho}} |\hat{\widetilde{S}}| \hat{\widetilde{S}}_{ij} - \Delta^2 \overline{\rho} |\widetilde{S}| \widetilde{S}_{ij} \right) \tag{14}$$

2.3. RANS Turbulence Modeling

The time average continuity and momentum equation counterparts of Equations (1) and (2) are given by Equations (15) and (16), respectively, with the velocities and other solution variables now representing ensemble-averaged (or time-averaged) values:

$$\rho \frac{\partial}{\partial x_i}(u_i) = 0 \tag{15}$$

$$\rho \frac{\partial}{\partial x_j}(u_i u_j) = -\frac{\partial p}{\partial x_i} + \frac{\partial}{\partial x_j}\left[\mu \left(\frac{\partial u_i}{\partial x_j} + \frac{\partial u_j}{\partial x_i} - \frac{2}{3}\delta_{ij}\frac{\partial u_l}{\partial x_l} \right) \right] + \rho \frac{\partial}{\partial x_j}\left(-\overline{u_i' u_j'} \right) \tag{16}$$

These two equations are known as the RANS equations, and the Reynolds stresses $(-\rho\overline{u_i' u_j'})$ must be modeled in order to close the RANS equations. A common method to relate the Reynolds stresses to the mean velocity gradients employs the Boussinesq hypothesis [65] expressed by Equation (17):

$$-\rho\overline{u_i' u_j'} = \mu_t \left(\frac{\partial u_i}{\partial x_j} + \frac{\partial u_j}{\partial x_i} \right) - \frac{2}{3}\left(\rho k + \mu_t \frac{\partial u_k}{\partial x_k} \right)\delta_{ij} \tag{17}$$

In the k-ε models and k-ω models, the Boussinesq hypothesis is applied to calculate the turbulent viscosity (μ_t). Thereupon, the several RANS turbulence models considered in this work are summarized, and the corresponding governing equations are presented.

2.3.1. Realizable *k*-*ε* Model

In the realizable *k*-*ε* model [66], the modeled transport equations for *k* and *ε* are given by Equations (18) and (19), respectively, where C_1 is calculated through Equation (20) and η is expressed by Equation (21). Note that Equation (18) still holds for the standard *k*-*ε* model, except for the model constants:

$$\frac{\partial}{\partial x_j}\left(\rho k u_j\right) = \frac{\partial}{\partial x_j}\left[\left(\mu + \frac{\mu_t}{\sigma_k}\right)\frac{\partial k}{\partial x_j}\right] + G_k + G_b - \rho\varepsilon - Y_M + S_k \tag{18}$$

$$\frac{\partial}{\partial x_j}\left(\rho\varepsilon u_j\right) = \frac{\partial}{\partial x_j}\left[\left(\mu + \frac{\mu_t}{\sigma_\varepsilon}\right)\frac{\partial\varepsilon}{\partial x_j}\right] + \rho C_1 S\varepsilon - \rho C_2 \frac{\varepsilon^2}{k + \sqrt{v\varepsilon}} + C_{1\varepsilon}\frac{\varepsilon}{k}C_{3\varepsilon}G_b + S_\varepsilon \tag{19}$$

$$C_1 = \max\left[0.43, \frac{\eta}{\eta + 5}\right] \tag{20}$$

$$\eta = \sqrt{2S_{ij}S_{ij}}\frac{k}{\varepsilon} \tag{21}$$

As an extra remark, it is important to mention that the enhanced wall treatment (EWT) was used with the realizable *k*-*ε* model. The EWT is a near-wall modeling method that consists of combining a two-layer model with enhanced wall functions. Note that if the near-wall mesh is fine enough to solve the viscous sublayer (commonly with the first near-wall node positioned at $y^+ \approx 1$), the enhanced wall treatment would be identical to the traditional two-layer zonal model [64].

2.3.2. Shear Stress Transport (SST) *k*-*ω* Model

The SST *k*-*ω* model [67] is more accurate and trustworthy for some flows than the standard and BSL *k*-*ω* models, such as adverse pressure gradient flows. More concretely, in the SST *k*-*ω* model, a limiter to the formulation of the eddy viscosity equation is used to attain the correct transport behavior, as expressed in Equation (22). In fact, since this model includes the benefits of both the Wilcox and *k*-*ε* models, and both models do not consider the turbulent shear stress's transport, the eddy viscosity is overestimated:

$$\mu_t = \frac{\rho k}{\omega}\frac{1}{\max\left[\frac{1}{\alpha^*}, \frac{SF_2}{a_1\omega}\right]} \tag{22}$$

All the additional model constants and equations for the turbulent kinetic energy and the specific dissipation rate are equal to the standard *k*-*ω* model, and they are presented in Equations (23) and (24), respectively:

$$\frac{\partial}{\partial x_i}\left(\rho k u_i\right) = \frac{\partial}{\partial x_j}\left(\Gamma_k\frac{\partial k}{\partial x_j}\right) + G_k - Y_k + S_k + G_b \tag{23}$$

$$\frac{\partial}{\partial x_i}\left(\rho\omega u_i\right) = \frac{\partial}{\partial x_j}\left(\Gamma_\omega\frac{\partial\omega}{\partial x_j}\right) + G_\omega - Y_\omega + D_\omega + S_\omega + G_{\omega b} \tag{24}$$

In these equations, Γ_k and Γ_ω represent the effective diffusivity of *k* and *ω*, while Y_k and Y_ω represent the dissipation of *k* and *ω* due to turbulence, respectively. Moreover, G_k represents the generation of turbulence kinetic energy due to the mean velocity gradients, and G_ω represents the generation of *ω*. More details of these terms and how they are calculated can be found in [64].

2.3.3. Reynolds Stress Model

The most complex RANS turbulence model is the Reynolds stress model (RSM). The RSM [68] offers greater potential than the previous models, since it abandons the isotropic

eddy viscosity hypothesis, closing the Reynolds-averaged Navier–Stokes equations by solving transport equations for the Reynolds stresses, together with an equation for the dissipation rate. In this way, it accounts for the influence of the streamline curvature, rotation, and quick changes in strain rate in a more rigorous approach and must be applied when the flow characteristics of interest are caused by anisotropy in the Reynolds stresses. However, the reliability of RSM predictions is restricted by the closure assumptions used to model various terms, such as the pressure strain and dissipation rate, sometimes reducing the RSM forecasts' accuracy.

In the linear pressure strain model, the turbulent diffusive transport ($D_{T,ij}$) is modeled by the simplified gradient diffusion model from [69], using a scalar turbulent diffusivity. Moreover, the EWT is also used with the RSM.

More details of these models and their implementation in Ansys Fluent as well as its validation can be found in [64].

3. Numerical Method

3.1. Unsteady 3D Models

The laminar unsteady computational study simulates the experimental results reported by Varieras et al. [35] and the LES in the experiments of Senter and Solliec [70]. Moreover, Figure 2 presents a schematic of the computational domain used in the DNS and LES studies.
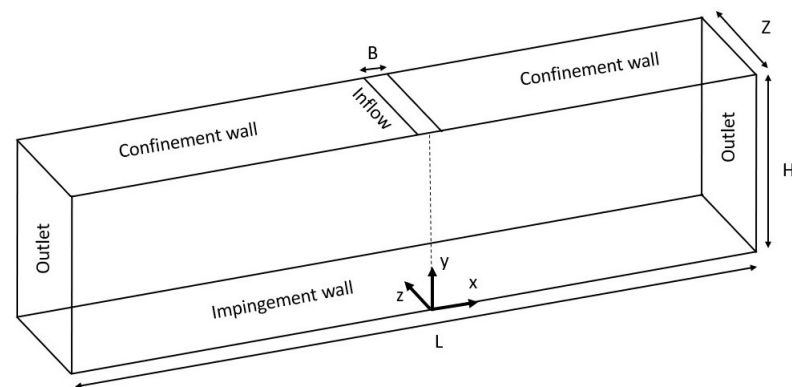

Figure 2. Schematic of the computational domain and boundary conditions used in unsteady laminar and LES studies.

The calculations were carried out using the FLUENT 16.2 solver. The convective term was discretized using a bounded central difference scheme, whereas the diffusive terms were discretized using a second-order central scheme. An implicit temporal discretization scheme was used, and the time step was defined such that the maximum CFL in the domain was $CFL < 1$ for LES and $CFL < 1$–10 for laminar DNS. After the flow starts its oscillatory behavior, the statistics were calculated for a sufficient number of oscillatory periods, which lead to a steady time-averaged velocity field. Along with the time averaging, all of the results presented were averaged in the homogeneous direction. At each time step, the solutions were assumed to be converged when the residuals of all the equations decreased by three orders of magnitude.

At the inflow, a mean velocity profile was specified for the turbulent jet as $V = V_j[1 - (x/(B/2))^7]$, where V_j was based on the value of the Reynolds number ($Re = V_j B / \nu$) and slot width (B) for each experimental work. However, for the laminar jet case, the profile was defined as $V = V_j[1 - (x/(B/2))^2]$. The fluctuations were produced in LES using the spectrum synthesizer method, which is based on the random flow generation technique originally proposed by Kraichnan [71] and modified by Smirnov et al. [72]. The fluctuating velocity components were calculated using this approach, which involves synthesizing a divergence-free velocity vector field from the sum of the Fourier harmonics.

Furthermore, the turbulence intensity must be defined, and a value of 9% was imposed, identical to that reported by Senter and Solliec [70].

Additionally, a non-slip boundary condition was applied on both walls of the computational domain. The outflow conditions were applied at the outlet. The outlet was kept at the same distance of the Senter and Solliec [70] work ($L = 100B$) and in line with the findings of Jaramillo et al. [57]. This distance was considered sufficiently large to avoid backflow at the outlets. Finally, periodic boundary conditions were imposed in the z direction. Indeed, periodic boundary conditions in the homogenous direction are only justifiable if the transverse dimension Z is large enough to capture the flow's greatest features. As a result, in a half-period ($Z/2$), the fluctuations must be substantially decorrelated. However, the transverse correlation data for several H/B ratios and the injection Reynolds numbers are not available, increasing the difficulty of selecting the optimum periodic domain size. In the literature, different lengths of the periodic domain have been used in the LES of impinging jet flows: $Z/B = \pi$ [73–76], $Z/B = 2$ [77,78], and $Z/B = 1$ [79]. Thus, a distance of $Z/B = \pi$ was considered, which is in line with the literature.

The mesh considered for the LES simulations was similar to the one used for the RANS simulations. This means that the x and y grid spacing was non-uniform in order to correctly characterize the strong gradient zones, with grid points concentrated around the wall and the jet's centerline. The mesh was uniform in the z direction. The distribution of the grid points was maintained to be as identical as possible from case to case. Overall, the meshes were created with a total of 3 million points. Since the mesh and the numerics are intertwined in LES, conducting a grid independence study to measure the mesh quality can be problematic. The criteria established by Piomelli and Chasnov [80], which set $\Delta x^+ < 100$, $\Delta y^+ < 2$, $\Delta z^+ < 30$ in the near-wall area for attached, wall-bounded flows were taken into consideration.

3.2. Steady 2D Model

The calculations were also carried out using the FLUENT 16.2 solver. The convection and diffusion terms were discretized using a second-order scheme. The solution was considered to attain convergence when the normalized residual of each variable was inferior to 10^{-6}.

Figure 1 shows a schematic diagram of the 2D turbulent confined slot jet emerging from a nozzle and impinging normally on a plate, while Figure 3 presents the computational domain of the present study. Since different experimental studies were considered, both the H/B ratios and slot widths B differed from case to case. The RANS computational study simulated the experimental results reported by Maurel and Solliec [81], Tu and Wood [13], Senter and Solliec [70], Ashforth-Frost et al. [15], and Zhe and Modi [14].
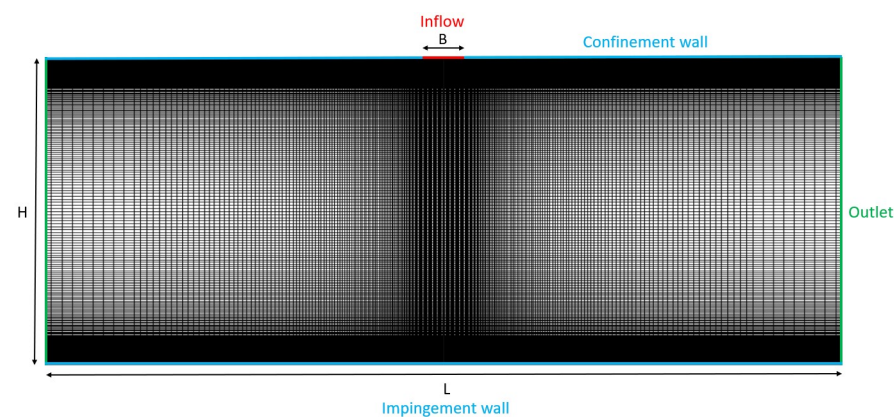

Figure 3. Schematic of the computational domain.

At the inflow, a mean velocity profile was specified which was similar to the one used in the LES simulations for the turbulent jet scenario, even though only half of it was used

due to the steady RANS symmetrical assumption. Moreover, the turbulent intensity was imposed in accordance with the data presented in each one of the experimental works. It was once more considered that $L = 100B$, a non-slip boundary condition was applied on both walls of the computational domain, and a symmetry boundary condition was applied at the symmetry line.

A non-uniform mesh was used in the present study, and 4 refinements were performed ranging from 25×10^3 to 200×10^3, considering only half of the domain presented in Figure 3. A mesh of 105×10^3 (350×300) was found to describe virtually identically to a mesh of 660×300 the strong gradient and complex regions, such as near the impingement surface, stagnation region, jet centerline, and wall jet. Once more, from case to case, the distribution of the grid points was maintained as identically as possible, but small adjustments were required to assure $y^+ \pm 1$ at the first grid points next to the impingement surface.

4. Results and Discussion

In this section, the dynamics of a laminar impinging jet is analyzed and validated with the literature (Section 4.1). Then, the performance of several RANS turbulence models is evaluated for various H/B ratios and compared with the available experimental data (Section 4.2). Subsequently, through LES, the dynamics of a turbulent impinging jet is analyzed (Section 4.3), paying particular attention to the non-stationarity of the flow, which can jeopardize the performance of some widely applied RANS turbulence models.

4.1. DNS Results

The self-sustained oscillations of a confined slot impinging jet—observed experimentally by Varieras et al. [35]—are predicted by 3D laminar unsteady simulations in this subsection. Varieras et al. [35] verified that the flow is steady for very confined jets, regardless of the Reynolds number. However, the dynamics was reported to be drastically different for less-constrained jets. In particular, the flow was found to bifurcate in the form of an oscillating flapping mode of the impinging jet above a certain Reynolds number. The H/B ratio's upper limit of the unconditional stability of the flow with respect to the flapping mode was found to be about 4.5. The Strouhal number was verified to be approximately 0.45, regardless of the aspect ratio or Reynolds number.

In this study, the geometric parameters B and H are equal to 0.005 m and 0.04 m, respectively, leading to an H/B ratio equal to 8. Two jet Reynolds numbers were considered (340 and 480), in line with [35]. According to the literature, these conditions should result in an unstable impinging jet presenting a sinuous oscillation mode.

For this, Figure 4 shows the flow visualization of a complete period for $Re = 340$ with a rate of 100 frames per second, and Figure 5 presents the vorticity magnitude at two extremes of the period, corresponding to insets (4) and (7) of Figure 4.

As expected, the results show that the impinging jet was unstable and developed a sinuous oscillation mode. More concretely, the development of a vortical zone formed by the jet vorticity in the region of the stagnation point, as well as the birth of a counter-rotating vortex emerging beneath the first (see Figure 5) by viscous interaction with the bottom wall, known as dipolar ejection, is notable. This phenomenon was periodic, and the same event occurred on the left side with respect to the unperturbed jet axis. Therefore, an oscillatory mode emerged that was characterized by a sinuous flapping motion of the emerging jet (see Figure 4) and the production and ejection of vortex dipoles. In particular, the jet's curvature changed, pointing toward both the recirculation zones, while the potential core zone remained practically unchanged. In addition, the sinuous instability caused a low-frequency oscillatory motion of the emerging jet, resulting in a sweeping of the impacted surface with the mentioned periodic dipole ejections alternately on each side. The same behavior was observed for $Re = 480$ (not shown).
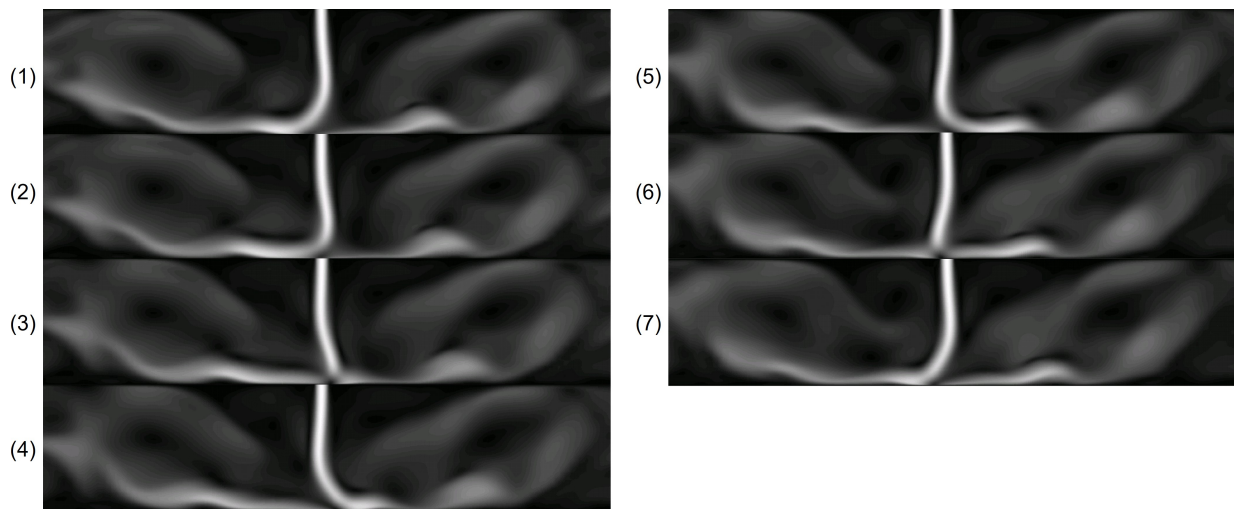
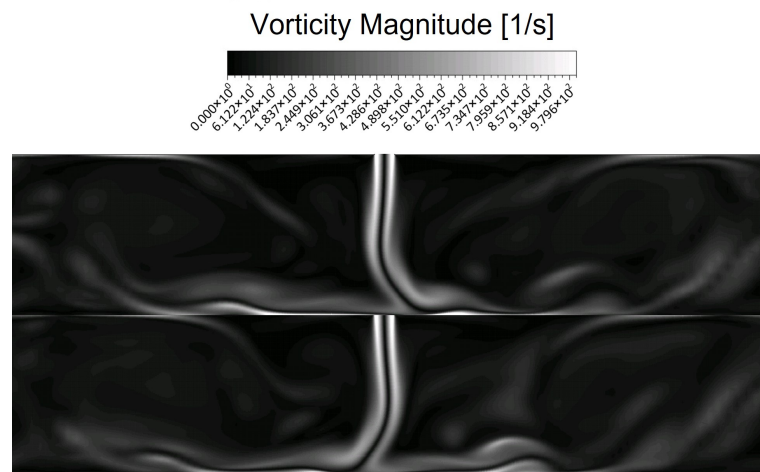**Figure 4.** Flow visualization of a complete period for $Re = 340$.

Figure 5. Vorticity magnitude at two extremes of a period for $Re = 340$.

Varieras et al. [35] found that the birth of the global oscillations is due to the amplification of frequencies produced by the inflexional instability of the wall jet by the impinging jet, with the wavelength being dependent on the width of the channel. Consequently, the impinging jet is susceptible to fluctuations caused by the wall jet, and global self-sustained oscillations arise.

To assess the frequency of these oscillations, three points were selected at the jet centerline: $y/B = 2$ (near the wall), $y/B = 4$ (mid-height of the channel), and $y/B = 6$ (near the jet's exit). Figure 6a,b represents the variation of the x velocity component during 1 s at $y/B = 4$ for $Re = 340$ and 480, respectively.

By analyzing Figure 6a,b, the frequencies could be determined—through the velocity signals—and were approximately equal to 15 Hz and 21 Hz for when Re was equal to 340 and 480, respectively. With the knowledge of these frequencies, the Strouhal number (defined as $St_H = fH/V_j$) was calculated, resulting in 0.451 for $Re = 340$ and 0.454 for $Re = 480$. Both values were close to 0.45, which fully agrees with the experimental results presented in [35]. Moreover, it is important to highlight that the choice of the point location did not influence the obtained results, since in the remaining two points, the frequency of the oscillations was the same (not shown). This illustrates that the sinuous oscillation mode was constant (in frequency) in all the jet's lengths.
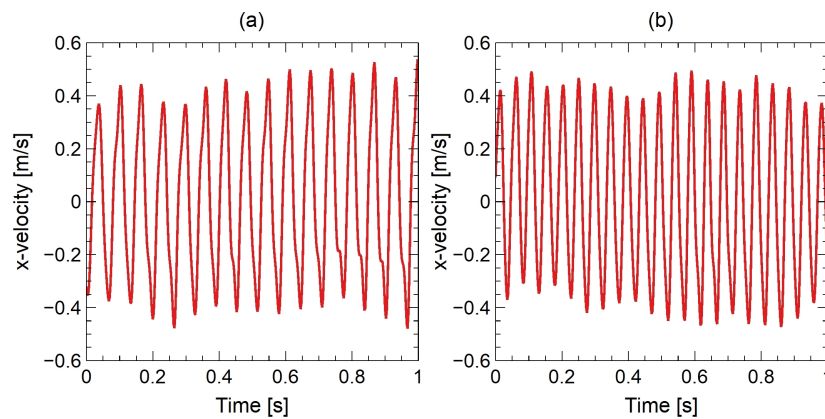
Figure 6. x velocity component during 1 s at $y/B = 4$ for (**a**) $Re = 340$ and (**b**) $Re = 480$.

In order to verify the effect of the jet's flapping in the time-averaged flow field, Figure 7a,b shows the velocity magnitude contours for the unsteady laminar simulation (time-averaged) and the steady laminar simulation, respectively. The difference between the two velocity contours is evident, particularly for the unsteady simulation, where the jet was broader close to the impingement wall and the recirculation zones were closer to the jet as a result of the jet's flapping.
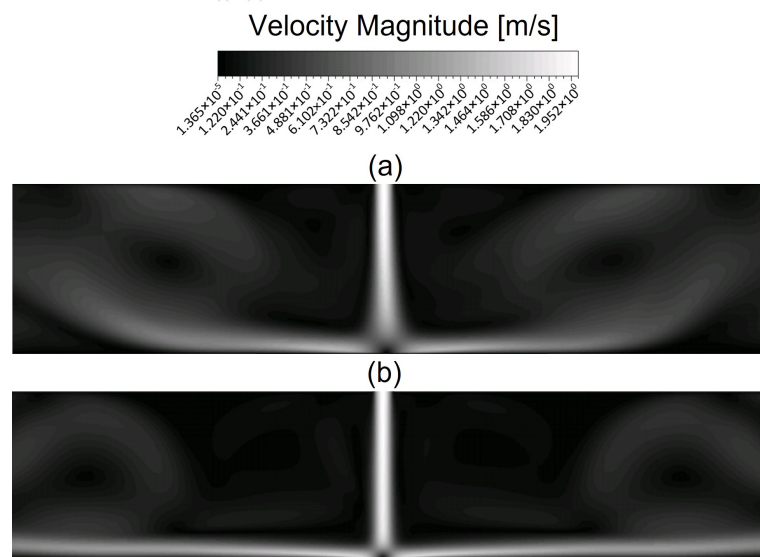
Figure 7. Velocity magnitude contours for (**a**) unsteady laminar (time-averaged) and (**b**) steady laminar.

4.2. RANS Results

Despite the correct prediction of the laminar jet's dynamics, almost all practical applications of an impinging jet are turbulent. For this, the correct prediction of this fluid flow is of extreme importance. In this subsection, the turbulent confined slot impinging jet is studied through the widely applied RANS simulations. In particular, the performances of several RANS turbulence models are compared with the experimental results of the literature, focusing on the influence of the H/B ratio on the models' accuracy.

4.2.1. Centerline y Velocity Component

The vertical velocity represented along the centerline is often used to characterize impinging jets. Figure 8a–c shows the distributions of the vertical velocity along the centerline obtained numerically with three RANS turbulence models for $H/B = 5$, 10, and 15, respectively, and for the same Reynolds number (2.7×10^4) considered in the experiments reported by Maurel and Solliec [81].
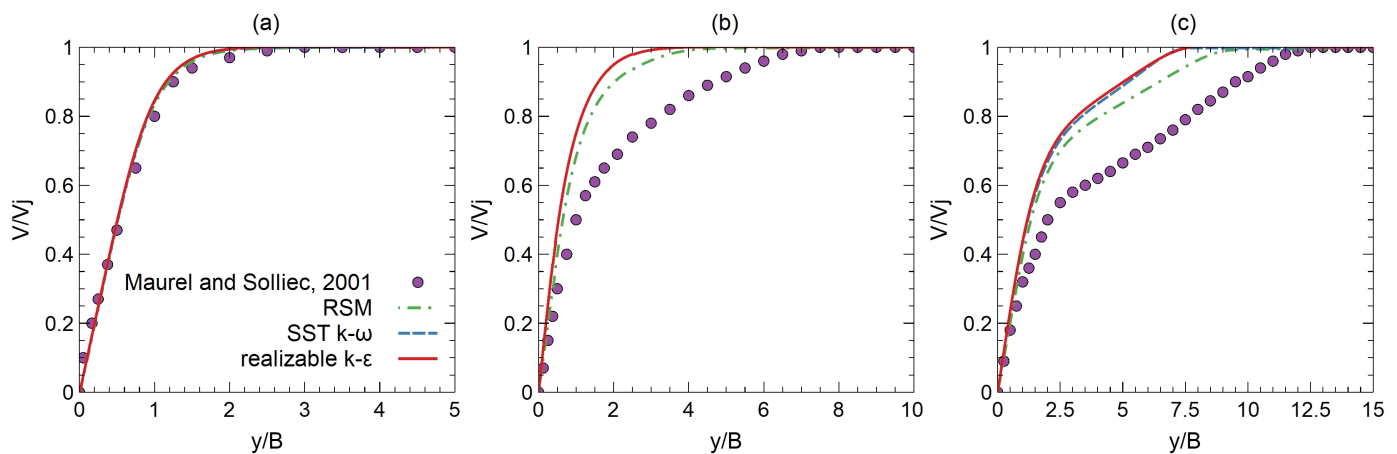
Figure 8. Centerline y velocity component profiles for (**a**) $H/B = 5$, (**b**) $H/B = 10$, and (**c**) $H/B = 15$, compared to reference results reported by Maurel and Solliec [81].

Maurel and Solliec [81] concluded that, except for the case of $H/B = 5$, the length of the potential core was almost constant and equal to approximately 4B, and the structure of the jet was highly influenced by the H/B ratio. In fact, for small confining H/B aspect ratios, the high static pressure in the stagnation area strongly affected the flow development up to the nozzle exit. Consequently, an enormous difference in the fluid flow existed, depending on the impingement plate being within the potential core of the jet or in the developing jet, and this has been clarified in the past by experimental measurements and LES calculations (see, e.g., [15,48,81,82]). For example, for the cases of $H/B = 5$ and 10, the expressions available in the literature for the relative length of the potential core were less accurate due to the strong confinement of the jet.

Very good agreement with the experimental data can be observed between the profiles of the vertical velocity using the three RANS turbulence models in the case of $H/B = 5$. However, as the H/B ratio increased, this agreement disappeared. For the cases of $H/B = 10$ and 15, the performance of the studied turbulence models was similar, and all of them overpredicted the experimental results. Moreover, the RSM performed better at predicting this velocity distribution, although it was still far from the experimental results, while the difference was more evident when considering the realizable k-ε and SST k-ω models.

These differences prove the inability of these models to predict the centerline y velocity component profiles for high H/B ratios. Kubacki and Dick [49] also showed that the results obtained with the RANS model are erroneous, since the length of the jet core is strongly overpredicted. The pointed explanation for this RANS model's performance relies on the poor production of turbulent kinetic energy [83]. On the other hand, Beaubert and Viazzo [46] as well as Dutta and Dewan [82], using LES, were able to match the velocity profiles with the ones presented by Maurel and Solliec [81] for $H/B = 10$.

4.2.2. C_f and Surface Pressure

The skin friction coefficient ($C_f = \tau_w / 0.5 \rho V_j^2$) distributions, predicted by the RANS turbulence models, along the impingement surface for $H/B = 12$ and $Re = 1.1 \times 10^4$ in $0 < x/B < 8$ are shown in Figure 9, and they were compared with the experimental results reported by Tu and Wood [13]. The skin friction coefficient is a non-dimensionalized representation of the drag force on the impingement surface.
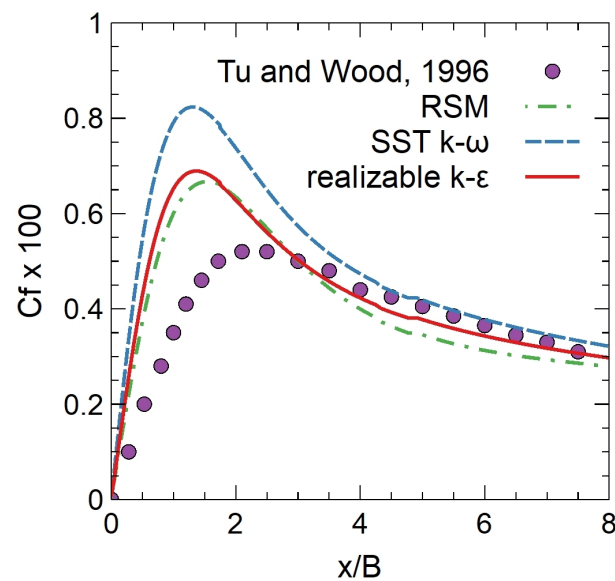
Figure 9. Skin friction coefficient profiles for $H/B = 12$, compared to reference results reported by Tu and Wood [13].

Overall, for $H/B = 12$, at the stagnation point, the skin friction coefficient had a minimum value of zero, implying that there was no streamwise flow over the impingement surface. Downstream of the stagnation point, the skin friction coefficient reached the peak value, attributed to a maximum streamwise velocity along the impingement wall. As the streamwise velocity was reduced, the skin friction coefficient monotonically declined.

Regarding the turbulence models' performance, for $H/B = 12$, all the turbulence models clearly failed at estimating both the magnitude and the location of the peak. The peak was located at $x/B = 1.5$ instead of $x/B = 2.5$ (experimental measurement), indicating that the turbulence models were not able to predict the higher diffusion of the jet that was verified experimentally.

Additionally, for $H/B = 12$, through the experimental pressure data reported by Tu and Wood [13] in the vicinity of the stagnation point, the stagnation area observed experimentally was broader than the one predicted by the RANS turbulence models (not shown). For an H/B ratio equal to 4, Achari and Das [19] found that the distribution of pressure followed the experimental data closely, but for a high H/B ratio (9), the results differed, especially in the region of $0.5 < x/B < 2$. Hence, the RANS turbulence models were not able to predict the higher diffusion of the jet that was verified experimentally.

4.2.3. Velocity Magnitude in the x Direction

As can be concluded from the previous results, at high H/B ratios, the turbulence models predicted narrower profiles in the x direction than the experimental ones. This inability of the turbulence models to predict the higher diffusion of the jet that was verified experimentally was even more striking when analyzing the velocity magnitude.

Figure 10a,b presents the normalized velocity magnitude profiles along the x direction at y/B equal to 4 (middle of the channel) and 1 (near the impingement surface), respectively, for an H/B ratio equal to 8 and a Reynolds number equal to 10^4. These data were compared with the experimental results presented by Senter and Solliec [70] for the case where the impingement plate was stationary.
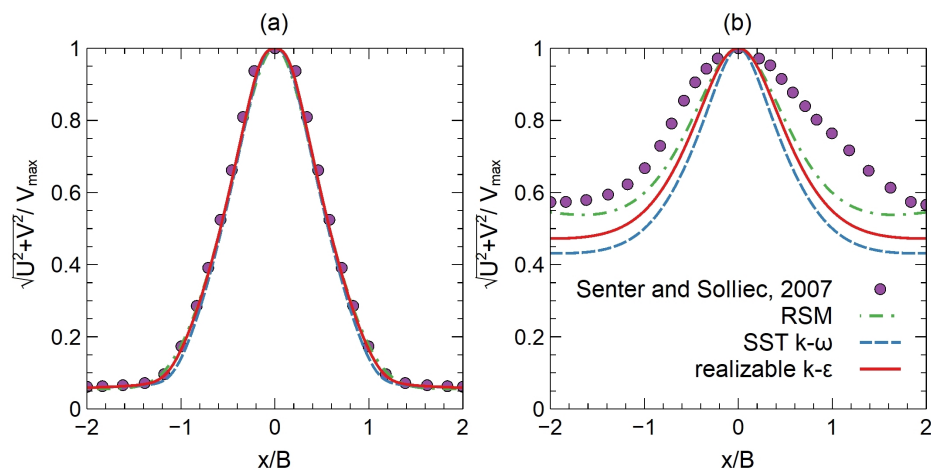
Figure 10. Normalized velocity magnitude between $-2 < x/B < 2$ for $H/B = 8$ at (**a**) $y/B = 4$ and (**b**) $y/B = 1$, compared to reference results reported by Senter and Solliec [70].

It is notable that the velocity profile at $y/B = 1$ was wider than at $y/B = 4$, since the further it was from the impingement plate, the smaller its effect on the jet structure. Specifically, close to the impingement plate, a strong streamline curvature was present, since the jet started to change from its initial position perpendicular to the impingement plate until it was parallel to it. Moreover, the growth of the shear layer of the jet as it approached the plate also added justification to the difference in both profiles.

When analyzing the performance of the RANS turbulence models, the numerical results were denoted to match exactly the experimental ones for $y/B = 4$, even though the results were disastrous for $y/B = 1$. Close to the impingement wall, the velocity magnitude profiles predicted by the turbulence models were, once more, narrower than the experimental profiles. Only the RSM could produce more accurate results, but they were still far from the ones reported by Senter and Solliec [70]. Once more, the inability of the turbulence models to predict the higher diffusion of the jet was verified in several time-averaged experimental studies.

4.2.4. Spanwise Velocity Profiles

Ashforth-Frost et al. [15] and Zhe and Modi [14] conducted detailed measurements of the spanwise velocity. While the former study focused on a Reynolds number of 2×10^4 and H/B distances of 4 (within the potential core of the jet) and 9.2 (beyond the potential core of the jet), the latter presented data for wider H/B distances and Reynolds numbers. In this study, the focus was on conditions that were common to both works. In particular, measurements were taken at non-dimensional spanwise points x/B near the impingement plate and were studied up to 5. Figures 11a–e and 12a–e show the streamwise velocity variation at different x/B locations for H/B ratios of 4 and 9.2, respectively.

Overall, for $H/B = 4$, both studies found that for $x/B = 1$, the near-wall velocity increased rapidly up to $y/B = 0.025$ and then continued to grow at increasing y/B distances, indicating contamination from the y velocity component within the stagnation area. This contamination might also explain a small difference in magnitude between the two profiles, since for the remaining x/B profiles, the results were nearly identical. The y/B distance across which this fast rise in velocity occurred increased as x/B increased, indicating the formation of the wall jet. At $x/B = 3$, the maximum near-wall velocity was achieved with $U/Vj = 0.98$. It was concluded that the wall jet was still growing, since the maximum velocity prevailed across a range of roughly $0.05 < y/B < 0.25$ above the plate. As the wall jet spread, beyond $x/B = 3$, the maximum velocity decreased. For $H/B = 9.2$, since the impingement wall lied beyond the potential core region of the jet, the velocity with which the jet impinged on the surface began to slow even before the wall was felt. For this reason, lower velocity values within the wall jet were found in both experiments for this H/B distance.
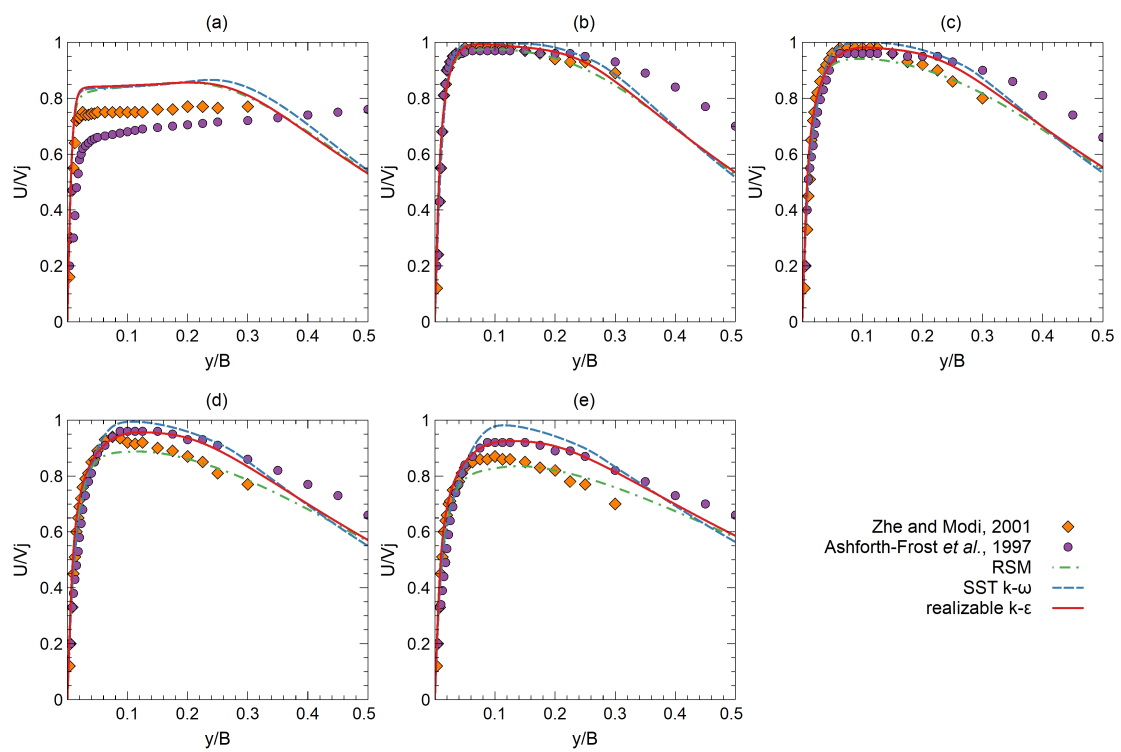
Figure 11. Spanwise velocity profiles for $H/B = 4$ at (**a**) $x/B = 1$, (**b**) $x/B = 2$, (**c**) $x/B = 3$, (**d**) $x/B = 4$, and (**e**) $x/B = 5$, compared to reference results reported by Ashforth-Frost et al. [15] and Zhe and Modi [14].
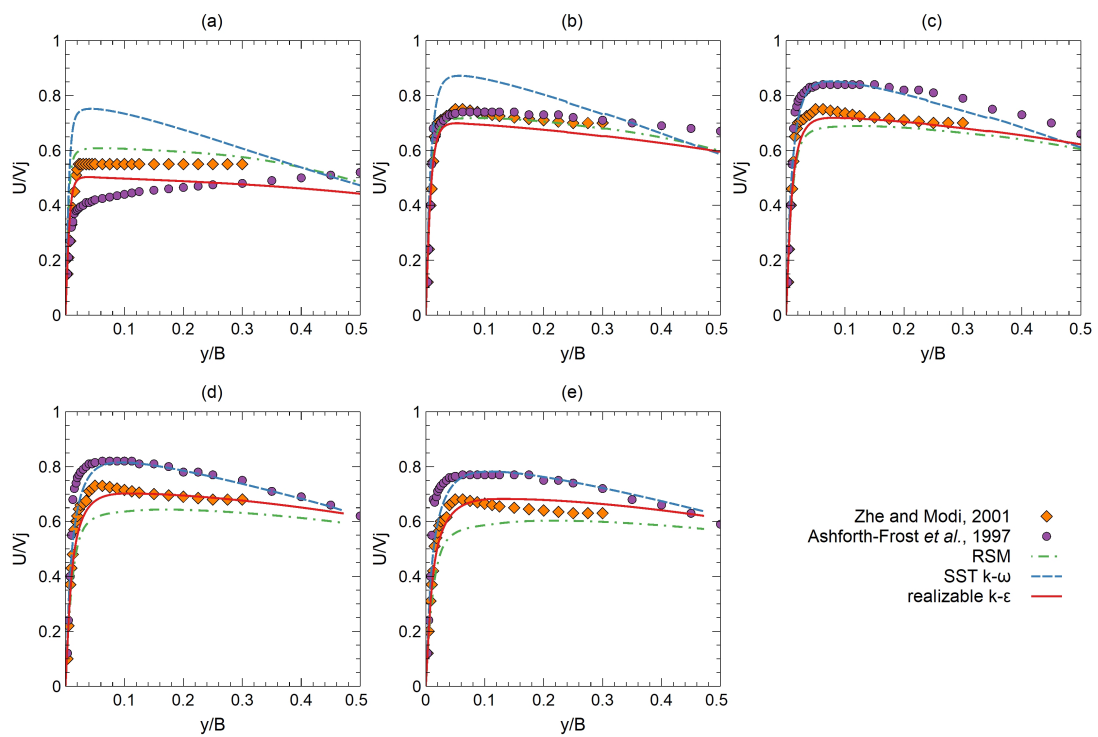

Figure 12. Spanwise velocity profiles for $H/B = 9.2$ at (**a**) $x/B = 1$, (**b**) $x/B = 2$, (**c**) $x/B = 3$, (**d**) $x/B = 4$, and (**e**) $x/B = 5$, compared to reference results reported by Ashforth-Frost et al. [15] and Zhe and Modi [14].

For $H/B = 4$, the computational results revealed that the three RANS turbulence models predicted similar results to the experiments, except for $x/B = 1$, due to the aforementioned reason. Moreover, for $x/B = 1, 2$, and 3, the three turbulence models predicted similar results between them. However, for the remaining two x/B distances, the RSM underpredicted the profiles when compared with the other models. Finally, Dutta and Dewan [18] also confirmed the good performance of the SST k-ω model for the case of $H/B = 4$, and Shukla and Dewan [48], using LES, were able to match closely the experimental results for $H/B = 4$.

For $H/B = 9.2$, the three RANS turbulence models predicted slightly different results. Specifically, the SST k-ω model always overpredicted the results (when compared with the remaining ones), while the realizable k-ε model underpredicted $x/B = 1$ and 2 and the RSM for $x/B = 3, 4$, and 5. Contrary to the previous case, none of the used models were able to match the experimental results for almost the entire range or predict the velocity at the close-wall region (until $y/B < 0.05$) for $x/B = 3, 4$, or 5. This failure also proves the inability of the models considered to predict the streamwise velocities for high H/B ratios. Additionally, Achari and Das [19] used four other different RANS turbulence models, and the same problem was noticed.

4.3. LES Results

As can be concluded from the previous results, all the studied turbulence models were proven to be satisfactory for small H/B ratios, such as $H/B \leq 5$, and failed when comparing several parameters with the available experimental data in the literature for high H/B ratios, such as $H/B = 8$. Moreover, as previously mentioned, Varieras et al. [35] defined $H/B \approx 4.5$ as the upper limit of the unconditional stability of the flow with respect to the flapping mode. Consequently, in this subsection, the LES results are analyzed with the aim of verifying if the flapping of the jet that occurs in the laminar case is also present at a higher Reynolds number and if this flapping justifies the failure of the RANS turbulence models for high H/B ratios. The LES study was conducted in accordance with the Senter and Solliec [70] experimental work. More concretely, the sizes of the geometry selected were $B = 0.02$ m and $H = 0.16$ m to achieve $H/B = 8$ (the same H/B ratio as in the laminar jet study), and the Reynolds number was defined as 10^4.

Figure 13 presents the flow visualization over a complete period, and Figure 14 shows the instantaneous vorticity magnitude at two extremes of a period.
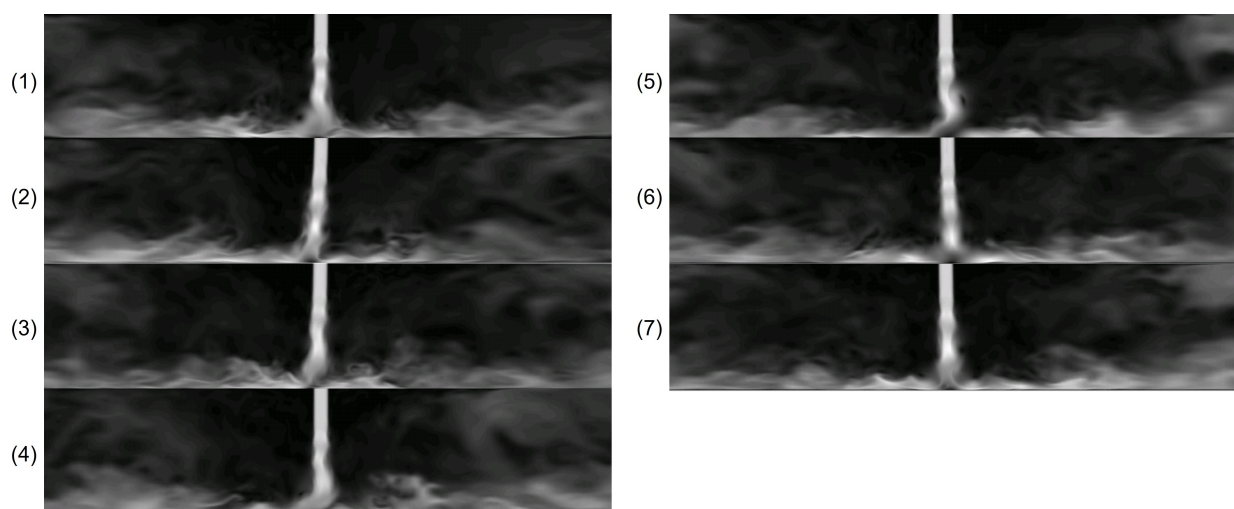

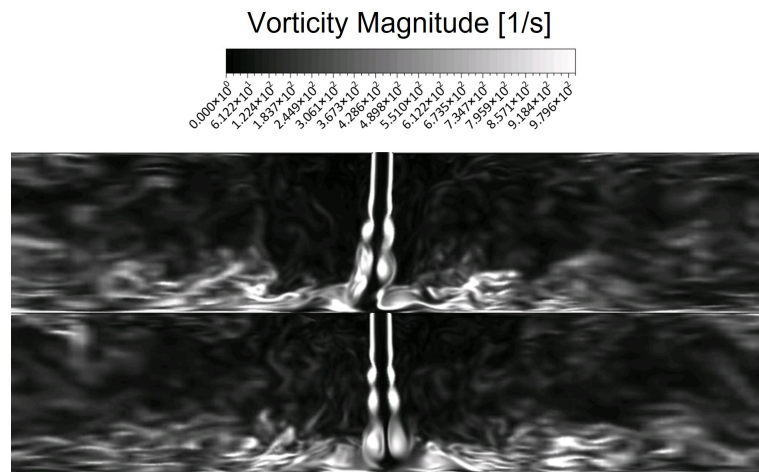**Figure 13.** Flow visualization of a complete period of oscillation.

Figure 14. Instantaneous vorticity magnitude at two extremes of a period.

The results show that the turbulent impinging jet was also unstable and developed a sinuous oscillation mode (see Figure 13). Figure 14 clearly exhibits the presence of bi-dimensional vortices generated by Kelvin–Helmholtz instabilities at the shear layer of the jet—which was also mentioned in previous LES studies [46,82]—as well as different scales of turbulence. The capture of the interaction between the Kelvin–Helmholtz vortices and the impinging wall is of extreme importance and is one of the roots of the flapping motion of the slot jets for the considered H/B ratio.

Figure 15 shows the instantaneous longitudinal x velocity component at the jet center-line and at $y/B = 4$ (mid-height of the channel) over 30 s, denoting a dominant frequency of the oscillations. This flapping motion presented an average frequency of 0.43 Hz, corresponding to a Strouhal number based on the jet nozzle ($St_B = fB/V_j$) of 1.1×10^{-3}. This value was equal to the one calculated with the data presented by Khayrullina et al. [11], who also reported on the flapping of a turbulent impinging jet for high H/B ratios.
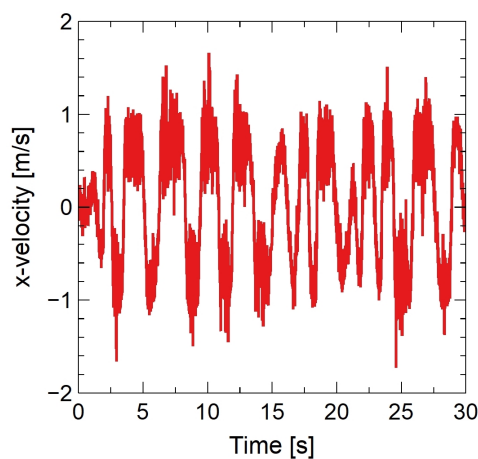

Figure 15. x velocity over 30 s for $Re = 10^4$ at $y/B = 4$.

Figure 16 presents the vertical velocity along the jet centerline predicted by LES. Moreover, Figure 17a,b presents the normalized velocity magnitude profiles along the x direction in the middle of the channel height ($y/B = 4$) and near the impingement surface ($y/B = 1$), respectively. Both results were compared with the experimental data presented by Senter and Solliec [70] for a stationary plate.
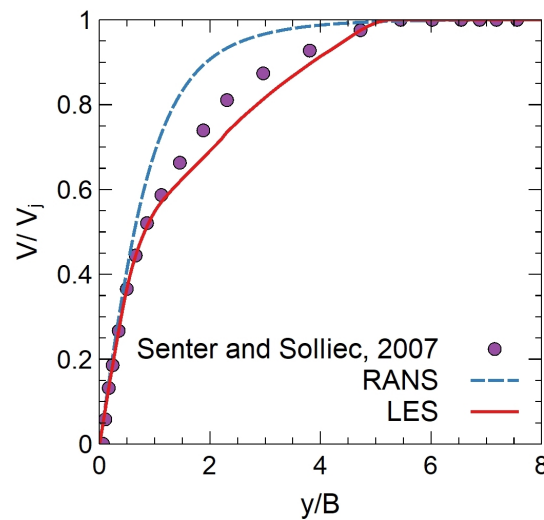
Figure 16. Centerline *y* velocity component profile, compared to reference results reported by Senter and Solliec [70].
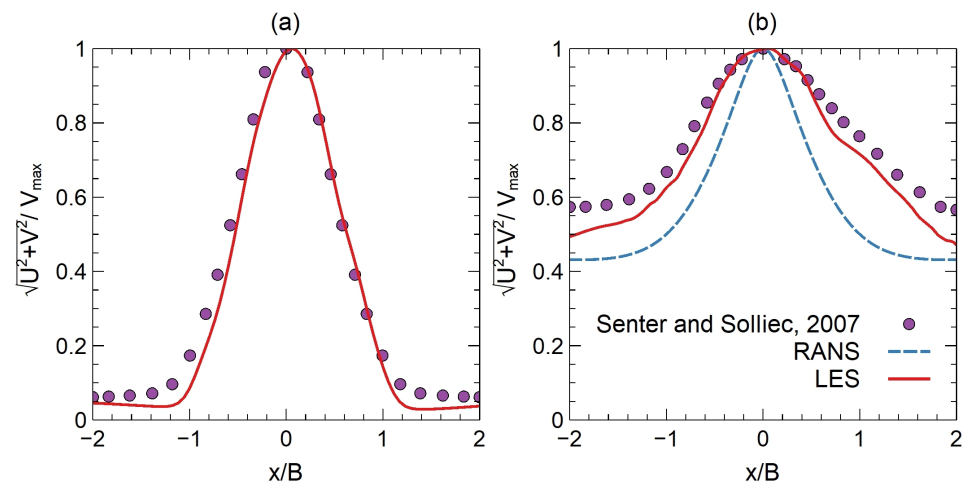

Figure 17. Normalized velocity magnitude between $-2 < x/B < 2$ at (**a**) $y/B = 4$ and (**b**) $y/B = 1$, compared to reference results reported by Senter and Solliec [70].

Through the analysis of Figure 16, it is possible to conclude that, contrary to the RANS turbulence model (SST *k-ω*), LES was able to predict precisely the length of the potential core of the jet, matching the experimental results reported by Senter and Solliec [70]. It slightly underpredicted the experimental results in the region of $2 < y/B < 4$. Nevertheless, similar poor results in this region while applying LES were also reported in [82].

By observing Figure 17a,b, it is possible to conclude that LES was also able to predict correctly both profiles, while the RANS turbulence models were only able to match the experimental results at $y/B = 4$ (far from the impingement plate), as concluded previously (see Figure 10). In particular, in Figure 17b, it is possible to verify the improvement of the LES profile compared with the one predicted by the RANS turbulence model (SST *k-ω*), proving RANS's inability to forecast the higher diffusion of the jet.

To further validate the LES results, Figure 18a,b presents the time-averaged, non-dimensional turbulent kinetic energy and the non-dimensional Reynolds stress, respectively, along the *x* direction at $y/B = 4$ (channel mid-height). The LES results presented in Figure 18a,b were compared with the experimental data reported by Senter and Solliec [70] as well as Maurel and Solliec [81], respectively.
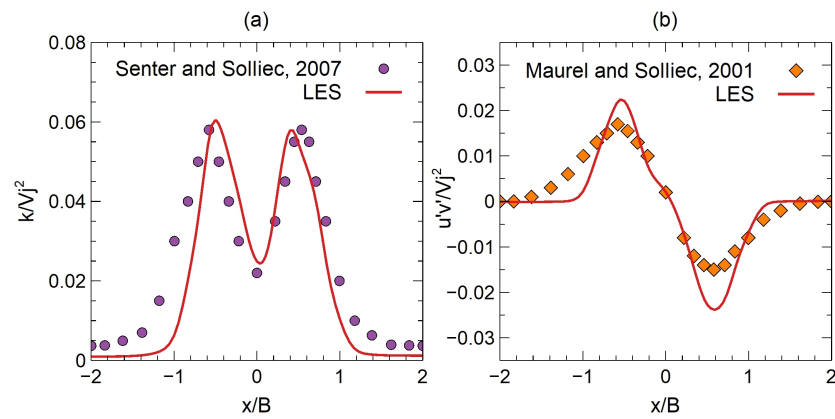
Figure 18. Normalized turbulent kinetic energy (**a**) and Reynolds stress (**b**) at $y/B = 4$, compared to reference results reported by Senter and Solliec [70] and Maurel and Solliec [81].

According to Figure 18a, the non-dimensional turbulent kinetic energy predicted by the LES simulation had a peak value of about 0.06, which was in very good agreement with the experimental results. Regarding the non-dimensional Reynolds stress (Figure 18b), the distribution along the x direction was in line with the experimental data despite the slight overprediction of the maximum value, similar to what was previously reported in the literature [49].

Figure 19a–c presents the LES time-averaged velocity field, the LES instantaneous velocity field, and the velocity field predicted by RANS (SST k-ω), respectively.
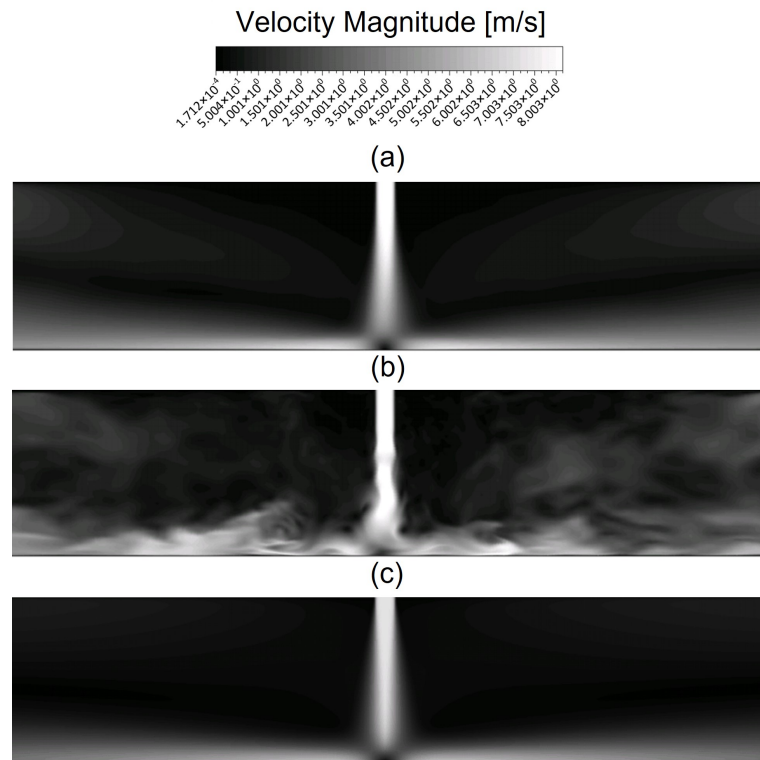

Figure 19. Velocity magnitude contours for (**a**) LES time-averaged, (**b**) LES instantaneous, and (**c**) RANS turbulence models.

First, it is notable that, similar to what was concluded in the laminar case (see Figure 7), as a result of the jet's flapping, the jet was much broader close to the wall when comparing the time-averaged field with the instantaneous velocity field. Moreover, when comparing the time-averaged LES with the RANS simulations, it became evident once more that RANS predicted a narrower jet profile close to the wall and a higher length of the potential core.

The previous results prove that the jet's flapping—observed for high H/B ratios—is one of the reasons that makes the RANS turbulence models incapable of matching the higher diffusion of the jet verified experimentally, requiring unsteady simulations to be able to predict this very complex phenomenon.

5. Conclusions

In this work, first, the dynamics of the laminar jet was studied. For an H/B ratio equal to 8, an unstable laminar impinging jet was observed featuring a sinuous oscillation mode (flapping motion) with a Strouhal number (based on H) of about 0.45, which was in full agreement with the literature.

Since almost all the impinging jet applications are turbulent, the performance of several RANS turbulence models was evaluated for various H/B ratios and compared with the available experimental data. For small H/B ratios, the RANS turbulence models were found to predict fairly well the centerline y velocity component distribution, the surface pressure profile, the velocity magnitude in the x direction, and the spanwise velocity profiles close to the impingement wall. On the other hand, for high H/B ratios, the RANS turbulence models overpredicted the size of the potential core, presenting poor matching with the experimental profiles of the centerline y velocity component. Moreover, it was concluded through the analysis of the profiles of the skin friction coefficient and velocity magnitude that the RANS turbulence models were not able to predict the higher diffusion of the jet, which was verified experimentally.

In fact, despite RANS having formed the core of industrial CFD applications for decades due to its low computational requirements, understanding the flow's transient behavior is essential. However, the RANS approach is insufficient in many circumstances, failing to forecast important flow behaviors such as the jet's flapping. Therefore, an LES study was conducted to investigate the dynamics of a turbulent jet. In particular, for an H/B ratio equal to 8, the mentioned flapping motion was also verified for a turbulent jet with a Strouhal number (based on B) of 1.1×10^{-3}. This flapping was established as one of the reasons that explains the higher diffusion close to the impingement wall verified in several time-averaged experimental studies. This unsteady behavior justifies the failure of the RANS turbulence models for high H/B ratios, while LES correctly computes this type of flow. Thus, the immediate use of this research is clear: steady RANS can be applied for confined impinging slot jets up to $H/B = 5$. For higher $H/B > 5$ values, LES must be conducted due to the unsteady flapping behavior that contributes to the ensemble-averaged quantities, as it cannot be captured by steady RANS models.

Author Contributions: Conceptualization, B.A.C.B., J.E.P.N. and J.C.F.P.; methodology, B.A.C.B.; software, B.A.C.B.; validation, B.A.C.B.; formal analysis, B.A.C.B.; investigation, B.A.C.B.; resources, J.E.P.N. and J.C.F.P.; data curation, B.A.C.B., J.E.P.N. and J.C.F.P.; writing—original draft preparation, B.A.C.B.; writing—review and editing, J.E.P.N. and J.C.F.P.; visualization, B.A.C.B.; supervision, J.E.P.N. and J.C.F.P.; project administration, J.C.F.P.; funding acquisition, J.C.F.P. All authors have read and agreed to the published version of the manuscript.

Institutional Review Board Statement: Not applicable.

Informed Consent Statement: Not applicable.

Data Availability Statement: Not applicable.

Conflicts of Interest: The authors declare no conflict of interest.

References

1. Han, B.; Goldstein, R. Jet-Impingement Heat Transfer in Gas Turbine Systems. *Ann. N. Y. Acad. Sci.* **2001**, *934*, 147–161. [CrossRef] [PubMed]
2. Pavlova, A.; Amitay, M. Electronic Cooling Using Synthetic Jets. *J. Heat Transf.-Trans. ASME* **2006**, *128*, 493–501. [CrossRef]
3. Polat, S. Heat and Mass Transfer in Impingement Drying. *Dry. Technol.* **1993**, *11*, 1147–1176. [CrossRef]
4. Martin, H. Heat and Mass Transfer Between Impinging Gas Jets and Solid Surfaces. *Adv. Heat Transf.* **1977**, *13*, 1–60. [CrossRef]
5. Jambunathan, K.; Lai, E.; Moss, M.; Button, B. A Review of Heat Transfer Data for Single Circular Jet Impingement. *Int. J. Heat Fluid Flow* **1992**, *13*, 106–115. [CrossRef]
6. Viskanta, R. Heat Transfer to Isothermal Gas and Flame Jets. *Exp. Therm. Fluid Sci.* **1993**, *6*, 111–134. [CrossRef]
7. van Hout, R.; Murugan, S.; Mitra, A.; Cukurel, B. Coaxial Circular Jets-A Review. *Fluids* **2021**, *6*, 147. [CrossRef]
8. Viegas, J.; Carrasco, L.; Pinto, L.; Morais, J.; Morais, P.; Aelenei, D. Full-Size Experimental Assessment of the Aerodynamic Sealing of Low Velocity Air Curtains. *Fluids* **2021**, *6*, 359. [CrossRef]
9. Foster, A.; Swain, M.; Barrett, R.; D'Agaro, P.; Ketteringham, L.; James, S. Three-dimensional effects of an air curtain used to restrict cold room infiltration. *Appl. Math. Model.* **2007**, *31*, 1109–1123. [CrossRef]
10. Viegas, J. Saltwater experiments with air curtains for smoke control in the event of fire. *J. Build. Eng.* **2016**, *8*, 243–248. [CrossRef]
11. Khayrullina, A.; Hooff, T.; Blocken, B.; van Heijst, G. PIV measurements of isothermal plane turbulent impinging jets at moderate Reynolds numbers. *Exp. Fluids* **2017**, *58*, 31. [CrossRef]
12. Thysen, J.H.; Hooff, T.; Blocken, B.; Heijst, G. PIV measurements of opposing-jet ventilation flow in a reduced-scale simplified empty airplane cabin. *Eur. J. Mech.-B/Fluids* **2022**, *94*, 212–227. [CrossRef]
13. Tu, C.; Wood, D. Wall pressure and shear stress measurements beneath an impinging jet. *Exp. Therm. Fluid Sci.* **1996**, *13*, 364–373. [CrossRef]
14. Zhe, J.; Modi, V. Near wall measurements for a turbulent impinging slot jet. *J. Fluids Eng. Trans. ASME* **2001**, *123*, 112–120. [CrossRef]
15. Ashforth-Frost, S.; Jambunathan, K.; Whitney, C. Velocity and turbulence characteristics of a semiconfined orthogonally impinging slot jet. *Exp. Therm. Fluid Sci.* **1997**, *14*, 60–67. [CrossRef]
16. Sangsom, W.; Inprasit, C. Design Parameters on Impingement Steam Jet Heat Transfer of Continuous Liquid Food Sterilization. *Fluids* **2022**, *7*, 185. [CrossRef]
17. Zhang, X.; Agarwal, R. Numerical Simulation of Fountain Formation due to Normal and Inclined Twin-Jet Impingement on Ground. *Fluids* **2020**, *5*, 132. [CrossRef]
18. Dutta, R.; Dewan, A. Comparison of various integration to wall (ITW) RANS models for predicting turbulent slot jet impingement heat transfer. *Int. J. Heat Mass Transf.* **2013**, *65*, 750–764. [CrossRef]
19. Achari, A.; Das, M. Application of various RANS based models towards predicting turbulent slot jet impingement. *Int. J. Therm. Sci.* **2015**, *98*, 332–351. [CrossRef]
20. Craft, T.; Graham, L.; Launder, B. Impinging Jet Studies for Turbulence Model Assessment—II. An Examination of the Performance of Four Turbulence Models. *Int. J. Heat Mass Transf.* **1993**, *36*, 2685–2697. [CrossRef]
21. Fernández, J.; Elicer-Cortés, J.; Valencia, A.; Pavageau, M.; Gupta, S. Comparison of low-cost two-equation turbulence models for prediction flow dynamics in twin-jets devices. *Int. Commun. Heat Mass Transf.* **2007**, *34*, 570–578. [CrossRef]
22. Jaramillo, J.; Perez Segarra, C.D.; Rodriguez, I.; Oliva, A. Numerical Study of Plane and Round Impinging Jets using RANS Models. *Numer. Heat Transf. Part B Fundam.* **2008**, *54*, 213–237. [CrossRef]
23. Tahsini, A.M.; Mousavi, S.T. Parametric Study of Confined Turbulent Impinging Slot Jets upon a Flat Plate. *Int. J. Aerosp. Mech. Eng.* **2012**, *6*, 2794–2798.
24. Hofmann, H.; Kaiser, R.; Kind, M.; Martin, H. Calculations of Steady and Pulsating Impinging Jets—An Assessment of 13 Widely used Turbulence Models. *Numer. Heat Transf. Part B-Fundam.* **2007**, *51*, 565–583. [CrossRef]
25. Schweikert, J.; Riedelsheimer, A.; Weigand, B. Numerical study of a turbulent impinging jet for different jet-to-plate distances using two-equation turbulence models. *Eur. J. Mech.-B/Fluids* **2016**, *61*, 210–217. [CrossRef]
26. Ramezanpour, A.; Mirzaee, I.; Firth, D.; Shirvani, H. A numerical heat transfer study of slot jet impinging on an inclined plate. *Int. J. Numer. Methods Heat Fluid Flow* **2007**, *17*, 661–676. [CrossRef]
27. Dewan, A.; Dutta, R. Recent Trends in Computation of Turbulent Jet Impingement Heat Transfer. *Heat Transf. Eng.* **2012**, *33*, 447–460. [CrossRef]
28. Popiel, C.; Trass, O. Visualization of a Free and Impinging Round Jet. *Exp. Therm. Fluid Sci.* **1991**, *4*, 253–264. [CrossRef]
29. Olsson, M.; Fuchs, L. Large Eddy Simulation of a Forced Semiconfined Circular Impinging Jet. *Phys. Fluids* **1998**, *10*, 476–486. [CrossRef]
30. Ozdemir, B.; Whitelaw, J. Impingement of an axisymmetric jet on unheated and heated flat plates. *J. Fluid Mech.* **1992**, *240*, 503–532. [CrossRef]
31. Liu, T.; Sullivan, J. Heat Transfer and Flow Structures in an Excited Circular Impinging Jet. *Int. J. Heat Mass Transf.* **1996**, *39*, 3695–3706. [CrossRef]
32. Goldschmidt, V.; Bradshaw, P. Flapping of a Plane Jet. *Phys. Fluids* **1973**, *16*, 354–355. [CrossRef]
33. Silva, C.; Metais, O. On the influence of coherent structures upon interactions in turbulent plane jet. *J. Fluid Mech.* **2002**, *473*. [CrossRef]

34. Ho, C.; Huerre, P. Perturbed Free Shear Layers. *Annu. Rev. Fluid Mech.* **2003**, *16*, 365–422. [CrossRef]
35. Varieras, D.; Brancher, P.; Giovannini, A. Self-sustained oscillations of confined impinging jet. *Flow Turbul. Combust.* **2007**, *78*, 1. [CrossRef]
36. Ho, C.M.; Nosseir, N. Dynamics of an Impinging Jet. Part 1. The Feedback Phenomenon. *J. Fluid Mech.* **1981**, *105*, 119–142. [CrossRef]
37. Didden, N.; Ho, C.M. Unsteady separation in a boundary layer produced by an impinging jet. *J. Fluid Mech.* **1985**, *160*, 235–256. [CrossRef]
38. Sakakibara, J.; Hishida, K.; Phillips, W. On the vortical structure in a plane impinging jet. *J. Fluid Mech.* **2001**, *434*, 273–300. [CrossRef]
39. El Hassan, M.; Nobes, D. Experimental Investigation of the Vortex Dynamics in Circular Jet Impinging on Rotating Disk. *Fluids* **2022**, *7*, 223. [CrossRef]
40. Chung, Y.; Luo, K. Unsteady Heat Transfer Analysis of an Impinging Jet. *J. Heat Transf.* **2002**, *124*, 1039–1048. [CrossRef]
41. Hadžiabdić, M.; Hanjalic, K. Vortical structures and heat transfer in a round impinging jet. *J. Fluid Mech.* **2008**, *596*, 221–260. [CrossRef]
42. Rohlfs, W.; Haustein, H.; Garbrecht, O.; Kneer, R. Insights into the local heat transfer of a submerged impinging jet: Influence of local flow acceleration and vortex-wall interaction. *Int. J. Heat Mass Transf.* **2012**, *55*, 7728–7736. [CrossRef]
43. Dairay, T.; Fortuné, V.; Lamballais, E.; Brizzi, L. Direct numerical simulation of a turbulent jet impinging on a heated wall. *J. Fluid Mech.* **2015**, *764*, 362–394. [CrossRef]
44. Aillaud, P.; Duchaine, F.; Gicquel, L.Y.M.; Didorally, S. Secondary peak in the Nusselt number distribution of impinging jet flows: A phenomenological analysis. *Phys. Fluids* **2016**, *28*, 095110. [CrossRef]
45. Hattori, H.; Nagano, Y. Direct numerical simulation of turbulent heat transfer in plane impinging jet. *Int. J. Heat Fluid Flow* **2004**, *25*, 749–758. [CrossRef]
46. Beaubert, F.; Viazzo, S. Large Eddy Simulations of plane turbulent impinging jets at moderate Reynolds numbers. *Int. J. Heat Fluid Flow* **2003**, *24*, 512–519. [CrossRef]
47. Bisoi, M.; Das, M.; Roy, S.; Patel, D. Large eddy simulation of three-dimensional plane turbulent free jet flow. *Eur. J. Mech.-B/Fluids* **2017**, *65*, 423–439. [CrossRef]
48. Shukla, A.; Dewan, A. OpenFOAM based LES of slot jet impingement heat transfer at low nozzle to plate spacing using four SGS models. *Heat Mass Transf.* **2019**, *55*, 911–931. [CrossRef]
49. Kubacki, S.; Dick, E. Simulation of plane impinging jets with k-ω based hybrid RANS/LES models. *Int. J. Heat Fluid Flow* **2010**, *31*, 862–878. [CrossRef]
50. Kubacki, S.; Rokicki, J.; Dick, E. Hybrid RANS/LES computations of plane impinging jets with DES and PANS models. *Int. J. Heat Fluid Flow* **2013**, *44*, 596–609. [CrossRef]
51. Wu, W.; Piomelli, U. Reynolds-averaged and wall-modelled large-eddy simulations of impinging jets with embedded azimuthal vortices. *Eur. J. Mech.-B/Fluids* **2015**, *55*, 348–359. [CrossRef]
52. So, H.; Yoon, H.; Chung, M. Large eddy simulation of flow characteristics in an unconfined slot impinging jet with various nozzle-to-plate distances. *J. Mech. Sci. Technol.* **2011**, *25*, 721–729. [CrossRef]
53. Dairay, T.; Fortuné, V.; Lamballais, E.; Brizzi, L. LES of a turbulent jet impinging on a heated wall using high-order numerical schemes. *Int. J. Heat Fluid Flow* **2014**, *50*, 177–187. [CrossRef]
54. Ghadi, S.; Esmailpour, K.; Hosseinalipour, S.; Mujumdar, A. Experimental Study of formation and development of Coherent Vortical Structures in Pulsed turbulent Impinging jet. *Exp. Therm. Fluid Sci.* **2015**, *74*, 382–389. [CrossRef]
55. Xu, B.; Wen, J.; Volkov, K. Large-eddy simulation of vortical structures in a forced plane impinging jet. *Eur. J. Mech.-B/Fluids* **2013**, *42*, 104–120. [CrossRef]
56. Esmailpour, K.; Bozorgmehr, B.; Hosseinalipour, S.; Mujumdar, A. Entropy generation and second law analysis of pulsed impinging jet. *Int. J. Numer. Methods Heat Fluid Flow* **2015**, *25*, 1089–1106. [CrossRef]
57. Jaramillo, J.; Trias, F.; Gorobets, A.; Perez Segarra, C.D.; Oliva, A. DNS and RANS modelling of a turbulent plane impinging jet. *Int. J. Heat Mass Transf.* **2012**, *55*, 789–801. [CrossRef]
58. Kim, K.; Min, Y.; Oh, S.; An, N.H.; Seoudi, B.; Chun, H.; Lee, I. Time-resolved PIV investigation on the unsteadiness of a low Reynolds number confined impinging jet. *J. Vis.* **2007**, *10*, 367–379. [CrossRef]
59. Chatterjee, A.; Tarbell, J. Laminar stability and heat transport in high aspect ratio planar confined impinging flows. *Int. J. Heat Mass Transf.* **2019**, *137*, 534–544. [CrossRef]
60. Chiriac, V.; Ortega, A. A numerical study of the unsteady flow and heat tranfer in a transitional confined slot jet impinging on an isothermal surface. *Int. J. Heat Mass Transf.* **2002**, *45*, 1237–1248. [CrossRef]
61. Smagorinsky, J. General Circulation Experiments with Primitive Equations. *J. Fluid Mech.* **1963**, *104*, 99–165. [CrossRef]
62. Lilly, D. A proposed modification of the Germano subgrid-scale closure. *Phys. Fluids A* **1994**, *4*, 633–635. [CrossRef]
63. Germano, M.; Piomelli, U.; Moin, P.; Cabot, W. A dynamic subgrid scale eddy viscosity model. *Phys. Fluids A* **1991**, *3*, 1760–1765. [CrossRef]
64. Ansys. *Ansys Fluent Theory Guide*; ANSYS, Inc.: Canonsburg, PA, USA, 2021.
65. Hinze, J.; Hinze, J. *Turbulence*; McGraw-Hill Classic Textbook Reissue Series; McGraw-Hill: New York, NY, USA, 1975.

66. Shih, T.H.; Liou, W.; Shabbir, A.; Yang, Z.; Zhu, J. A New k-ε Eddy Viscosity Model for High Reynolds Number Turbulent Flows. *Comput. Fluids* **1995**, *24*, 227–238. [CrossRef]
67. Menter, F. Two-Equation Eddy-Viscosity Turbulence Models for Engineering Applications. *AIAA J.* **1994**, *32*, 1598–1605. [CrossRef]
68. Launder, B.; Reece, G.; Rodi, W. Progress in the Development of a Reynolds Stress Turbulence Closure. *J. Fluid Mech.* **1975**, *68*, 537–566. [CrossRef]
69. Daly, B.; Harlow, F. Transport Equations in Turbulence. *Phys. Fluids* **1970**, *13*, 2634–2649. [CrossRef]
70. Senter, J.; Solliec, C. Flow field analysis of a turbulent slot air jet impinging on a moving flat surface. *Int. J. Heat Fluid Flow* **2007**, *28*, 708–719. [CrossRef]
71. Kraichnan, R. Diffusion by a Random Velocity Field. *Phys. Fluids* **1970**, *13*, 22–31. [CrossRef]
72. Smirnov, A.; Shi, S.; Celik, I. Random Flow Generation Technique for Large Eddy Simulations and Particle-Dynamics Modeling. *J. Fluids Eng.* **2001**, *123*, 359–371. [CrossRef]
73. Voke, P.; Gao, S.; Leslie, D. Large-eddy simulations of plane impinging jets. *Int. J. Numer. Methods Eng.* **1995**, *38*, 489–507. [CrossRef]
74. Voke, P.R.; Gao, S. Numerical study of heat transfer from an impinging jet. *Int. J. Heat Mass Transf.* **1998**, *41*, 671–680. [CrossRef]
75. Tsubokura, M.; Kobayashi, T.; Taniguchi, N.; Jones, W. A numerical study on the eddy structures of impinging jets excited at the inlet. *Int. J. Heat Fluid Flow* **2003**, *24*, 500–511. [CrossRef]
76. Hoffmann, G.; Benocci, C. Numerical simulation of spatially-developing planar jets. In Proceedings of the 74th Fluid Dynamics Symposium on Application of Direct and Large Eddy Simulation of Transition and Turbulence, Adelaide, Australia, 10–14 December 1994; Volume 26.
77. Cziesla, T.; Biswas, G.; Chattopadhyay, H.; Mitra, N. Large-eddy simulation of flow and heat transfer in an impinging slot jet. *Int. J. Heat Fluid Flow* **2001**, *22*, 500–508. [CrossRef]
78. Rhea, S.; Bini, M.; Fairweather, M.; Jones, W. RANS modelling and LES of a single-phase, impinging plane jet. *Comput. Chem. Eng.* **2009**, *33*, 1344–1353. [CrossRef]
79. Yu, M.; Chen, L.; Jin, H.; Fan, J. Large eddy simulation of coherent structure of impinging jet. *J. Therm. Sci.* **2005**, *14*, 150–155. [CrossRef]
80. Piomelli, U.; Chasnov, J.R. Large-Eddy Simulations: Theory and Applications. In *Turbulence and Transition Modelling: Lecture Notes from the ERCOFTAC/IUTAM Summerschool Held in Stockholm, 12–20 June 1995*; Springer: Dordrecht, The Netherlands, 1996; pp. 269–336. [CrossRef]
81. Maurel, S.; Solliec, C. A turbulent plane jet impinging nearby and far from a flat plate. *Exp. Fluids* **2001**, *31*, 687–696. [CrossRef]
82. Dutta, R.; Dewan, A. LES of a Turbulent Slot Impinging Jet to Predict Fluid Flow and Heat Transfer. *Numer. Heat Transf. Part A Appl.* **2013**, *64*, 759–776. [CrossRef]
83. Kubacki, S.; Dick, E. Convective heat transfer prediction for an axisymmetric jet impinging onto a flat plate with an improved k-ω model. *Int. J. Numer. Methods Heat Fluid Flow* **2009**, *19*, 960–981. [CrossRef]